NATIONAL MOSAIC AND MULTI-SENSOR QPE (NMQ) SYSTEM
Description, Results, and Future Plans

BY JIAN ZHANG, KENNETH HOWARD, CARRIE LANGSTON, STEVE VASILOFF, BRIAN KANEY, AMI ARTHUR, SUZANNE VAN COOTEN, KEVIN KELLEHER, DAVID KITZMILLER, FENG DING, DONG-JUN SEO, ERNIE WELLS, AND CHUCK DEMPSEY

A research system integrates radar, rain gauge, satellite, and numerical weather prediction data and generates automated, seamless national 3D radar mosaic and multisensor quantitative precipitation estimates at high temporal and spatial resolution.

T he deployment of the U.S. Weather Surveillance Radar-1988 Doppler (WSR-88D) network (Crum and Alberty 1993; www.roc.noaa.gov/) has provided meteorologists with critical information toward the issuance of warnings for tornadoes, severe storms, and flash floods. In the early years, the users were able to access only two-dimensional (2D) imagery products from single radar or multiradar mosaic instead of the full 3D base-level data in real time because of

AFFILIATIONS: ZHANG, HOWARD, VASILOFF, VAN COOTEN, AND KELLEHER—NOAA/OAR/NSSL, Norman, Oklahoma; LANGSTON, KANEY, AND ARTHUR—CIMMS/University of Oklahoma, Norman, Oklahoma; KITZMILLER, DING, AND SEO—NOAA/NWS/OHD, Silver Spring, Maryland; WELLS—NOAA/NWS/OCWWS, Silver Spring, Maryland; DEMPSEY—Salt River Project, Tempe, Arizona
CORRESPONDING AUTHOR: Jian Zhang, NOAA/National Severe Storms Laboratory, 120 David L. Boren Blvd., Norman, OK 73072
E-mail: jian.zhang@noaa.gov

The abstract for this article can be found in this issue, following the table of contents.
DOI:10.1175/2011BAMS-D-11-00047.1

In final form 23 May 2011
©2011 American Meteorological Society

limited bandwidth for transmitting data. The advent of Internet-2 and effective compression techniques made it possible to transmit base-level radar data from the WSR-88D network economically and in real time, as demonstrated by the Collaborative Radar Acquisition Field Test (CRAFT) Project (Droegemeier et al. 2002; Kelleher et al. 2007). In 2003, the U.S. National Weather Service (NWS) implemented the communication infrastructure that facilitated the central collection and distribution of base-level data in real time from more than 140 WSR-88D sites to several centralized hubs (Crum et al. 2003a,b; www. roc.noaa.gov/NWS_Level_2/AMS.asp). Now the real-time data are available to users from government agencies, universities, and private industries. The success of the project opened many new opportunities for multiradar and multisensor applications in meteorology, aviation, and hydrology. For instance, free access to the volume scan base-level data allows users to build 3D and 4D multiradar mosaics on a regional to national scale (e.g., Zhang et al. 2005; Lakshmanan et al. 2006; Langston et al. 2007), providing more complete depictions and rendering of storm structure than previous 2D products. Further, the radar mosaic grid is easily combined with information from other data sources such as satellite, gridded model analyses,

AMERICAN METEOROLOGICAL SOCIETY — OCTOBER 2011 BAMS | 1321

or forecast fields, increasing the value of radar data in the overall forecast and warning process (e.g., Gourley et al. 2001, 2002; Xu et al. 2008).

The National Mosaic and Multi-Sensor Quantitative Precipitation Estimation (QPE) (NMQ) system is a multiradar, multisensor system built upon the CRAFT data network. The objectives of NMQ research and development (R&D) are to assimilate different observational networks toward creating 1) high-resolution national multisensor QPEs for flash flood and flood warnings and water resource management and 2) high-resolution national 3D grids of radar reflectivity (Z) for data assimilation, numerical weather prediction model verification, and aviation product development. The system ingests base-level data from more than 140 WSR-88D radars and about 31 Canadian C-band weather radars and generates 3D radar reflectivity mosaic and QPE products in real time over the conterminous United States (CONUS). In addition, the NMQ system ingests Rapid Update Cycle (RUC; Benjamin et al. 2004) model analysis fields and Hydrometeorological Automated Data System (HADS; www.nws.noaa.gov/oh/hads/WhatIsHADS.html) gauge data for various multisensor QPE algorithms.

The NMQ system is fully automated and has been running in real time since June 2006. The system generates high-resolution 3D reflectivity mosaic grids (31 vertical levels) and a suite of severe weather and QPE products for the CONUS at a 1-km horizontal resolution and 2.5-min update cycle. Currently, the system keeps a running 3-yr product archive online (http://nmq.ou.edu). The experimental products are provided to users from government agencies, universities, research institutions, and the private sector in real time and have been utilized in various meteorological, aviation, and hydrological applications. Further, the NMQ system has a Web-based evaluation tool that ingests a number of operational QPE products generated from different sensors (radar, gauge, and satellite), where the NMQ experimental products are compared with the operational products and with independent gauge observations in real time. The Web-based verification system is accessible to the NWS forecasters and to the general public. Feedbacks from the forecasters and public provided valuable guidance for the R&D of NMQ. Through these interactions, the NMQ system facilitates advances of hydrometeorological sciences and technologies in a real-time environment and serves as a test bed for rapid science-to-operation infusion. This paper describes the scientific components of the NMQ system and presents the initial evaluation results and future development plans of the system.

SYSTEM OVERVIEW. The NMQ system was established in distributive computation architecture with four major modules. A simple overview flowchart of the NMQ system is shown in Fig. 1. Multiple data sources are used in all four major modules that constitute the NMQ system: 1) single radar processing; 2) 3D and 2D radar mosaic; 3) the next-generation QPE (Q2; Vasiloff et al. 2007), and 4) evaluation. Data sources include the level-2 (base-level) data from the WSR-88D network, the Environment Canada weather radar network, RUC model hourly analyses, lighting data, HADS, and regional rain gauge networks. Descriptions of each module are provided below.

Single radar processes. There are four scientific algorithms in the single radar processing: 1) reflectivity quality control (QC), 2) vertical profile of reflectivity (VPR), 3) single radar Cartesian (SRC) grid, and 4) single radar hybrid scan reflectivity (HSR).

REFLECTIVITY QUALITY CONTROL. The base-level radar reflectivity data are quality controlled to remove nonprecipitation echoes, including those from clear air, biological targets (birds, bats, and insects), sun strobes, residual ground clutter, electronic interference, and anomalous propagation (AP). The reflectivity QC module includes preprocessing, a
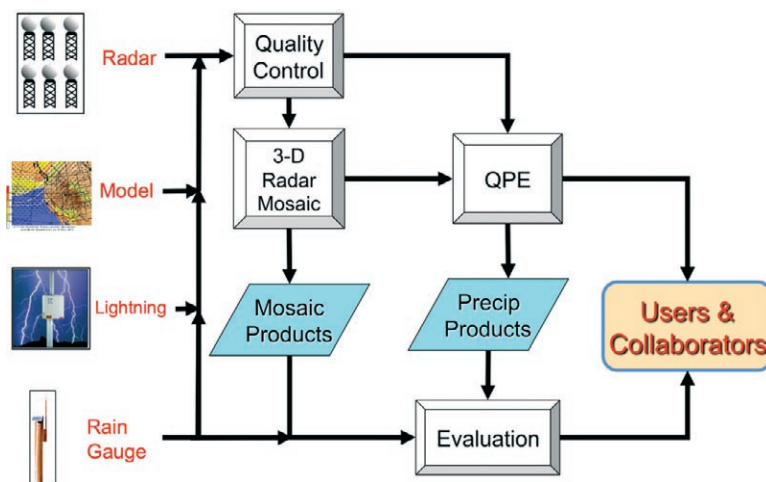

FIG. 1. An overview flowchart of the NMQ system.

neural network, and postprocessing. The neural network approach is based on 3D spatial characteristics of reflectivity (Lakshmanan et al. 2007, 2010), such as intensity, gradients, texture, and depth of radar echoes. All the reflectivity bins with significant blockages or are too close to the terrain (i.e., if the bottom of the bin is within 50 m of the ground) are removed in the preprocessing. The pre- and post-processing utilize spatial and temporal image filters and heuristic rules (e.g., Zhang et al. 2004) based on radar scan mode and environmental data to remove specific nonprecipitation echoes, such as speckles, sun strobes (Figs. 2a,b), clear air, and biological returns. For instance, total areas of radar echoes above a certain intensity in two consecutive volume scans are compared. If the difference (increase) between the echo areas in the two volume scans exceeds a certain threshold, then the second volume scan is considered to contain a hardware-testing signal [e.g., false echoes around KMBX (Minot, North Dakota) radar in Fig. 2c] and the data are discarded (Fig. 2d). Another example of the heuristic rules is for removing the so-called bloom echoes that are returns from migrating insects, birds, bats, and anomalous propagation (AP)
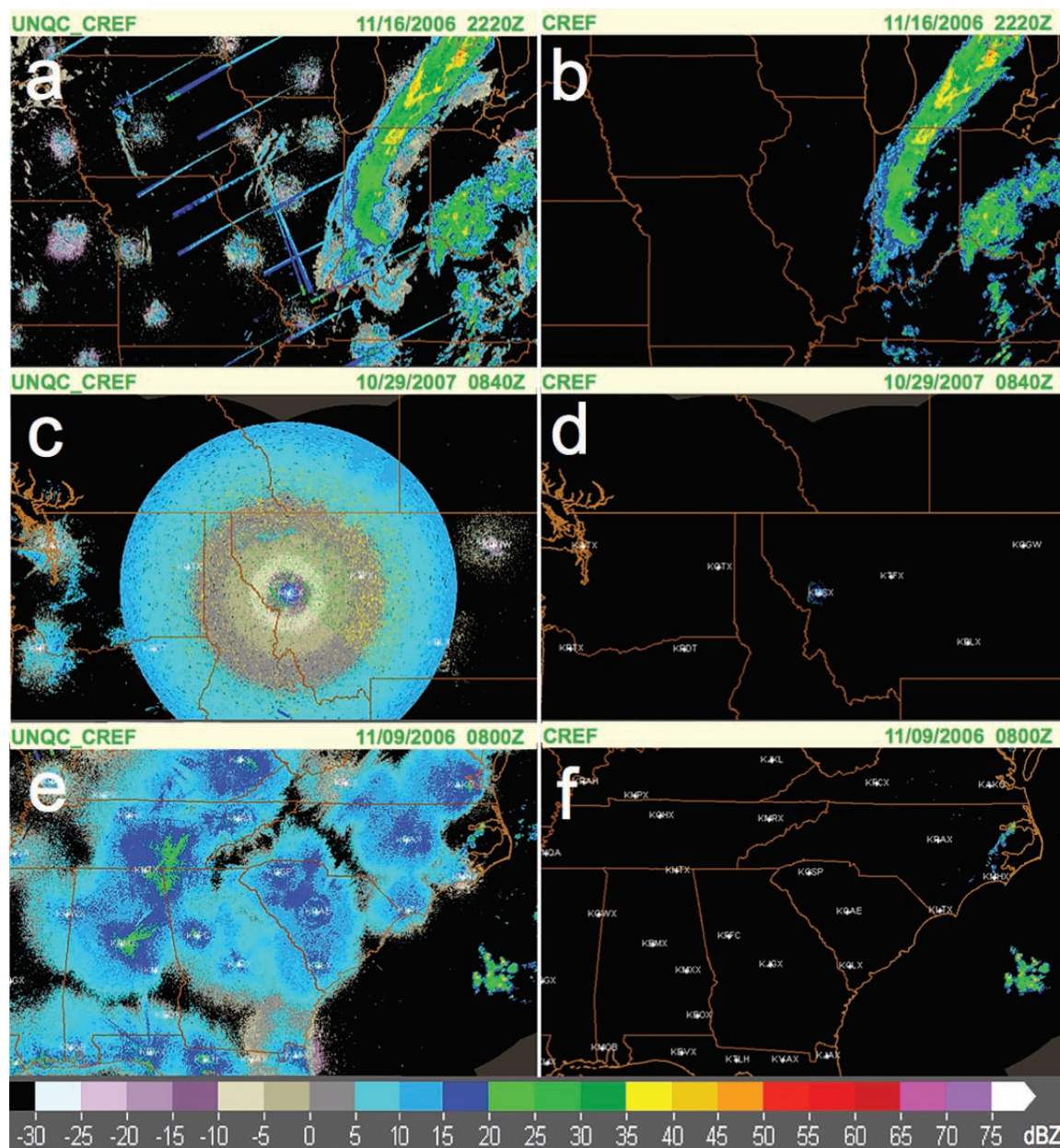

FIG. 2. Composite reflectivities (a),(c),(e) before and (b),(d),(f) after the QC. Composite reflectivities are valid at (a),(b) 2220 UTC 16 Nov 2006, (c),(d) 0840 UTC 29 Oct 2007, and (e),(f) 0800 UTC 9 Nov 2006.
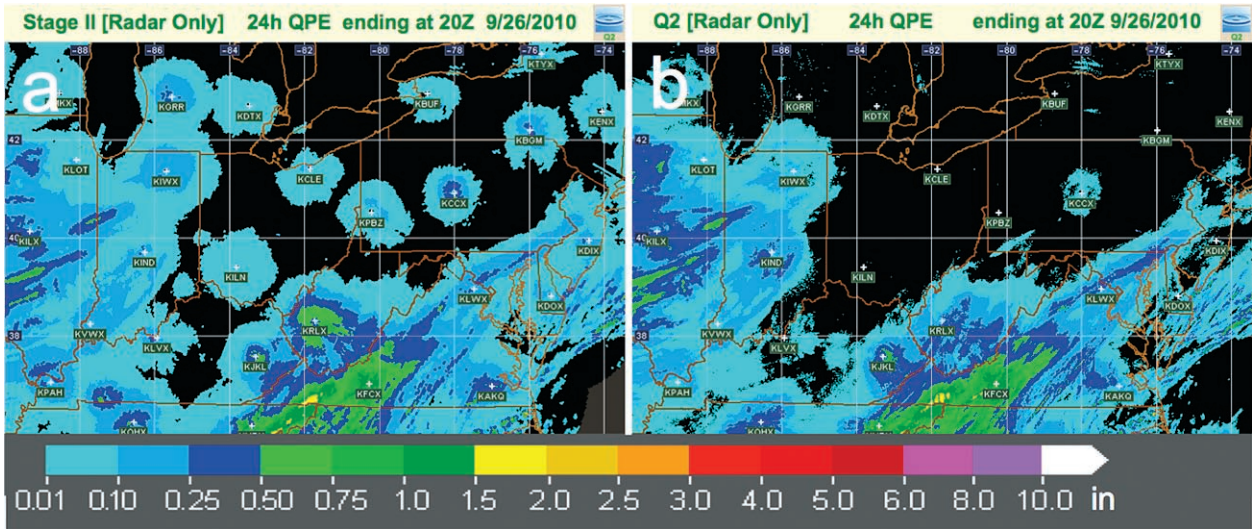
FIG. 3. (a) Stage II and (b) NMQ 24-h radar-based rainfall accumulations ending at 2000 UTC 26 Sep 2010.

due to nocturnal radiation cooling near the surface. When a radar is operating in clear-air modes and the surface temperature at the radar site is above 5°C, all the echoes in the volume scan are removed (Figs. 2e,f). The heuristic rules together with the neural network greatly reduce nonprecipitation echoes in the radar rainfall products. Figure 3 shows the NWS operational stage II (Lin and Mitchell 2005) radar-based 24-h rainfall accumulations and the NMQ accumulations ending at 2000 UTC 26 September 2010. The stage II products are the default input to the NWS Multi-Sensor Precipitation Estimator (MPE; Glaudemans et al. 2008) system and show considerable bloom echo contamination (Fig. 3a). The bloom echoes have been largely removed by the NMQ system (Fig. 3b).

Different types of radars are handled individually in the NMQ single radar quality assurance process before their reflectivity data are integrated into the mosaic grid. For instance, a statistical clutter removal module was developed for the Canadian radars to remove persistent ground clutters in the lower tilts. Also, specific quality assurance modules will be developed for C-band and X-band radars to address the attenuation issue. These processes allow NMQ flexibilities to integrate different radar networks while using common modules beyond the single radar process.

SINGLE RADAR CARTESIAN GRID. Each volume scan of a quality-controlled reflectivity field is interpolated from the native spherical coordinate system onto a 3D Cartesian grid that is centered at the radar site and is in a cylindrical equidistant map projection. For WSR-88D radars, the Cartesian grid covers a 460-km range for coastal radars and a 300-km range for inland radars. It has a horizontal resolution of 0.01° (~1 km × 1 km), and 31 levels ranging from 500 m to 18 km above mean sea level (MSL). The analysis scheme includes a nearest-neighbor mapping on the range–azimuth plane and an exponential
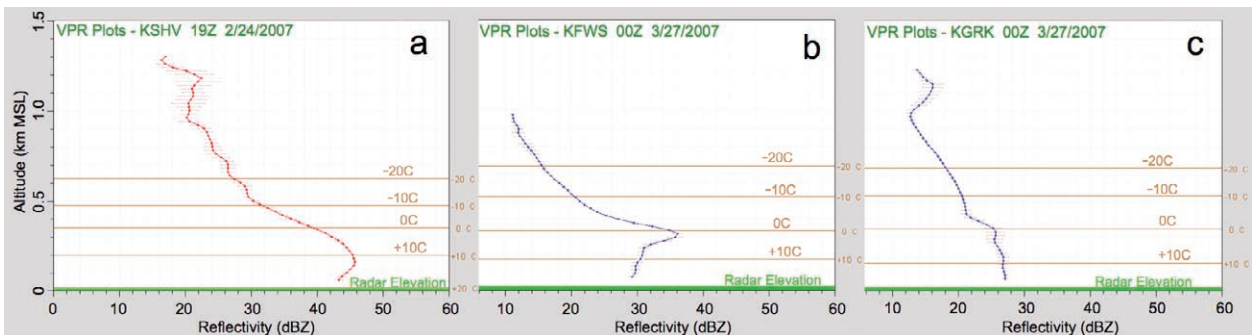

FIG. 4. Example VPRs for (a) convective, (b) stratiform, and (c) tropical precipitation. The horizontal brown lines indicate, from top to bottom, −20°, −10°, 0°, and 10°C temperature heights at the radar sites.
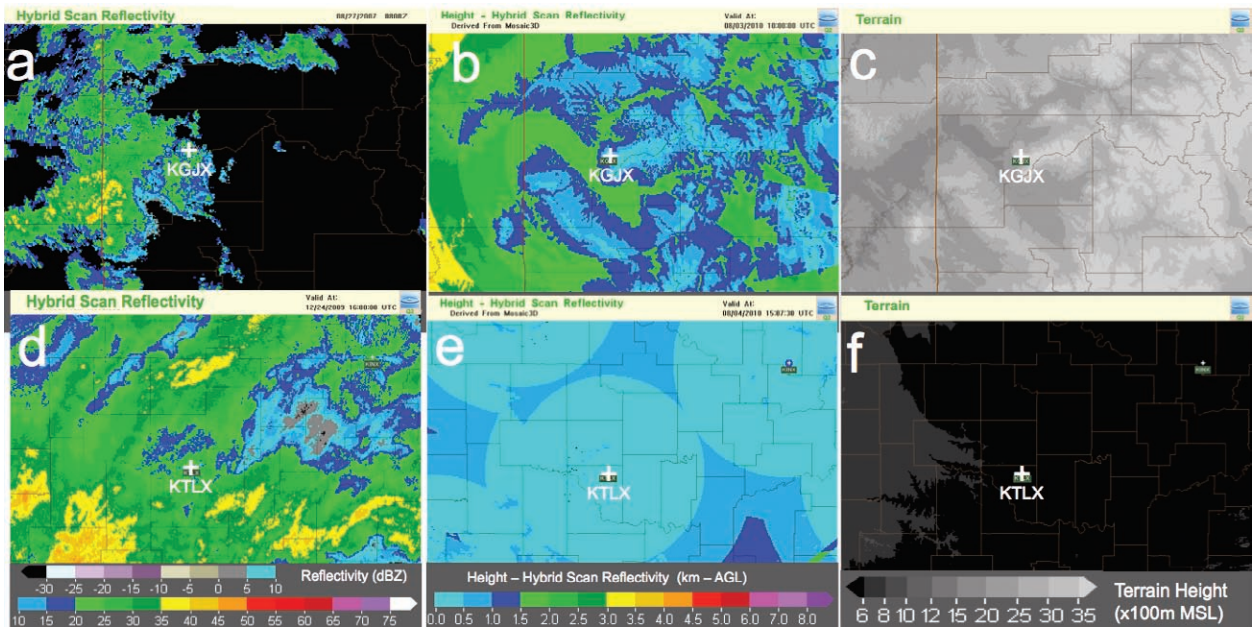
Fig. 5. (a),(d) Example hybrid scan reflectivity and (b),(e) associated height fields from (a),(b) KGJX (Grand Junction) and (d),(e) KTLX (Oklahoma City). The hybrid scan height field represents the bottom of the lowest radar beams that are less than 50% blocked. (c),(f) Corresponding terrain fields.

interpolation in the elevation direction (Zhang et al. 2005; Lakshmanan et al. 2006). No extrapolation was applied at the top and bottom of the radar volume scan beyond half a beam width.

Vertical profiles of reflectivity. VPRs are derived from the quality-controlled reflectivity in its native coordinates. A detailed discussion about the computation of VPRs can be found in Zhang et al. (2008). The VPRs are critical in the identification of warm-rain processes and producing more accurate QPEs (Xu et al. 2008). Example VPRs for different types of precipitation regimes are shown in Fig. 4. The convective VPR (Fig. 4a) shows a maximum in reflectivity above the lifting condensation level at ~1.5 km (above mean sea level, based on a nearby sounding), representing the coalescence growth of large rain droplets (sometimes hailstones) in the convective clouds. Below the lifting condensation level, the reflectivity decreases with decreasing height probably because of evaporations. The warm-rain VPR (Fig. 4c), on the other hand, shows gradually increasing reflectivity with the decreasing height all the way to the surface, representing a continued growth of a large number of medium-sized raindrops in a very moist environment (Xu et al. 2008).

A brightband (BB) feature is shown in the stratiform VPR as a peak near the freezing level (0°C height) (Fig. 4b). For cool-season stratiform precipitation, radar-derived QPEs often show large overestimation

where the lowest radar beams are sampling the bright band and underestimation where the beams are sampling the ice region above the bright band. These errors can be mitigated through various corrections for the nonuniform VPRs (e.g., Koistinen 1991; Kitchen et al. 1994; Vignal et al. 1999, 2000; Seo et al. 2000; Germann and Joss 2002; Bellon et al. 2005). In the NMQ system, a correction for the brightband effects is applied in real time using the approach developed by Zhang and Qi (2010). Further studies for the correction of radar rainfall estimation in areas where the beam samples the ice region are underway.

SINGLE RADAR HYBRID SCAN REFLECTIVITY. From quality-controlled single radar reflectivity data, the lowest (altitude) radar bins with valid reflectivity values are found. These constitute a 2D field that is equivalent to the hybrid scan reflectivity (HSR) in O'Bannon (1997) and Fulton et al. (1998). The HSR field consists of different beam heights at different locations, because the height of the radar beam increases with range. Further, beam blockages and terrain heights vary spatially. Generally, the higher the HSR bin is, the less accurate the radar-based precipitation estimates, because of nonuniform vertical profiles of reflectivity. Figure 5 shows example HSR and the associated height fields from KGJX (Grand Junction, Colorado) and KTLX (Oklahoma City, Oklahoma) radars. Because the KGJX radar is situated on a mountaintop (3,061 m above MSL), the lowest available reflectivity
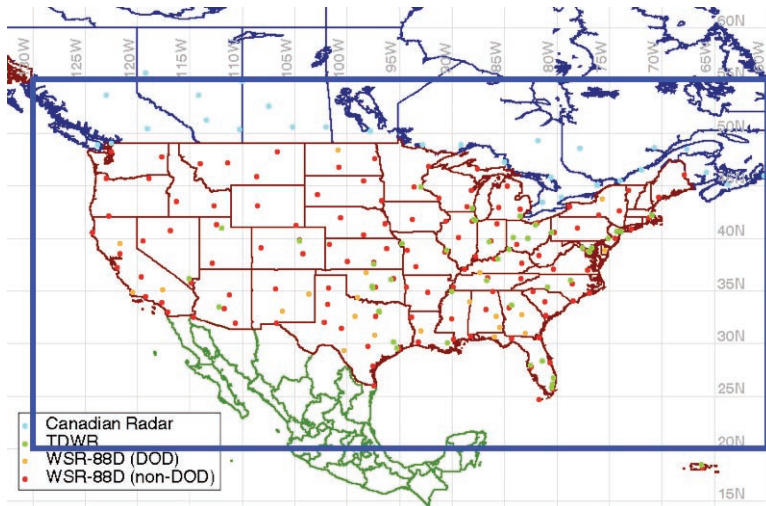
FIG. 6. NMQ product domain (solid blue box). Dots of different colors represent different radar networks including WSR-88D (red and brown), TDWR (green), and the operational Canadian weather radars (cyan).

observations are 1–2 km above the ground on average (Fig. 5b). For shallow stratiform precipitation events, the KGJX radar may only observe the top parts of the precipitating clouds or may even overshoot the cloud tops, resulting in rainfall underestimation. The KTLX radar, on the other hand, is located on flat land, and the radar network is denser in the area than around KGJX. As a result, most of the lowest observations in the KTLX vicinity are within 1 km above the ground (Fig. 5e). This indicates, in general, that the rainfall estimates from the KTLX radar would be more accurate than those from KGJX.

Three-dimensional reflectivity mosaic and severe storm products. Single radar 3D reflectivity Cartesian grids from multiple radars are combined into a 3D reflectivity mosaic grid that covers the CONUS and the southern part of Canada (Fig. 6). The mosaic domain spans from 130° to 60°W in longitude and from 20° to 55°N in latitude. The grid is in the cylindrical equidistant map projection and has a resolution of 0.01° (latitude) × 0.01° (longitude). The resolution in the east–west direction is approximately 1.045 km at the southern bound of the domain and about 0.638 km at the northern bound of the domain. The resolution in the north–south direction is about 1.112 km everywhere. An exponential distance weighting function is used when multiple radar

observations cover a single grid cell (Zhang et al. 2005). Figure 7 shows a horizontal and a vertical cross section taken from the 3D reflectivity mosaic grid for the Dallas hailstorm on 5 May 1995. The 3D reflectivity grid depicts several convective cells at different stages of their life cycles.

The NMQ system is designed to be flexible to integrate different radar networks. In the current NMQ system at the National Severe Storms Laboratory (NSSL), real-time data from 31 Canadian radars, two terminal Doppler weather radars (TDWR), and one television station radar are ingested. Other efforts are ongoing to incorporate mobile radar observations [e.g., those from the National Oceanic and Atmospheric Administration (NOAA) Hydrometeorological Testbed (HMT); http://hmt.noaa.gov] as well as gap-filling radars, such as those from Collaborative Adaptive Sensing of Atmosphere (CASA; McLaughlin et al. 2005).

A suite of severe storm products, including probability of severe hail (POSH; Witt et al. 1998), maximum expected hail size (MEHS; Witt et al. 1998), 18-dBZ echo top (ETP), vertically integrated liquid (VIL; Greene and Clarke 1972), and VIL density (VILD; Amburn and Wolf 1997), are calculated from the 3D reflectivity mosaic grid and the RUC 3D temperature analysis. Figure 8 shows examples of the aforementioned products for a hailstorm that occurred in Wabasha County, Minnesota, on 13 September 2007. The 3D reflectivity grid in
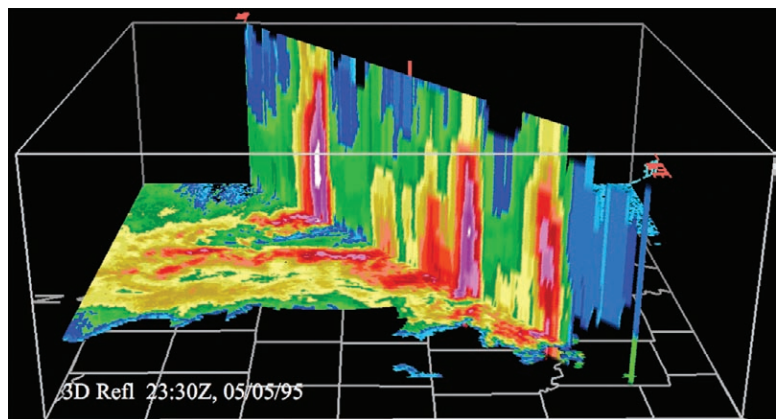

FIG. 7. Horizontal and vertical cross sections from the 3D reflectivity mosaic of the Dallas hail storm on 5 May 1995.
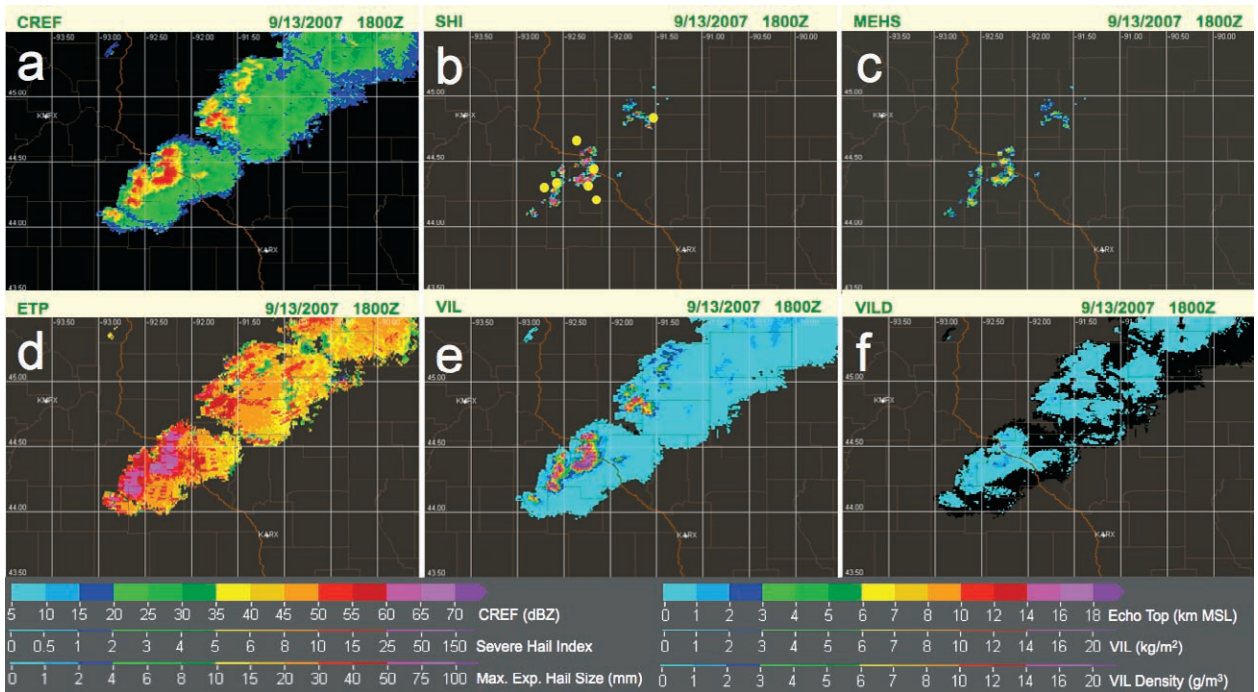
FIG. 8. Example 2D severe storm products from the NMQ system for a hailstorm on 13 Sep 2007 near the Minnesota–Wisconsin boundary. The products include (a) CREF, (b) severe hail index (SHI), (c) maximum expected hail size (MEHS), (d) ETP of 18 dBZ or higher, (e) VIL, and (f) VILD. Surface hail reports (yellow dots) from the NWS Storm Prediction Center (www.spc.noaa.gov/climo/reports/yesterday.html) are overlaid on the top of the SHI field in (b).

conjunction with the environmental 3D thermal field is also used to identify microphysical processes and to segregate precipitation regimes. A detailed discussion of the classification of precipitation regimes will be given in the next section.

Next-generation QPE. Q2, a key component in the NMQ system, performs automated precipitation classification and generates multisensor precipitation products ranging from instantaneous rates to 72-h accumulations. The multisensor product suite includes radar-based QPE; local gauge bias-corrected radar QPE; gauge-only QPE; and a QPE combining gauge, orography, and precipitation climatology. Details of each QPE product are presented below.

MOSAIC OF HYBRID SCAN REFLECTIVITY. The radar-based Q2 is computed from the radar HSR. Single radar HSR fields are mosaicked to produce a regional HSR field. The HSR mosaic scheme and associated weighting functions are defined below:

$$\text{HSR} = \frac{\sum_i w_L^i \times w_H^i \times \text{SHSR}^i}{\sum_i w_L^i \times w_H^i}, \tag{1}$$

$$w_L = \exp\left(\frac{d^2}{L^2}\right), \tag{2}$$

and

$$w_H = \exp\left(-\frac{h^2}{H^2}\right). \tag{3}$$

Here, HSR represents the mosaicked hybrid scan reflectivity, *i* is the radar index, and SHSR is the single radar hybrid scan reflectivity field. There are two components in the weighting function, one for the horizontal w_L and another for the vertical w_H. The variable *d* represents the distance between the analysis point and the radar, and *h* represents the height (above mean sea level) of the single radar HSR bin. The parameters *L* and *H* are scale factors of the two weighting functions, respectively. This mosaic scheme yields QPE fields with better horizontal continuity than does a nearest-neighbor approach, because the latter can result in discontinuities in mosaicked data fields midway between neighboring radars. The discontinuities are due to factors including different calibration among the radars and different sampling paths from the radars to the overlapping mosaic region.

CLASSIFICATION OF PRECIPITATION REGIMES. The accuracy of radar precipitation rate is largely dependent on the choice of a proper Z and rainfall rate (R; Z–R) relationship for precipitation at a given location and given time. In the current operational WSR-88D rainfall algorithm (Fulton et al. 1998), one Z–R relationship is applied to the radar domain (230 km × 230 km). The choice of the Z–R relationship is set at the local forecast office level, and a challenge exists in providing real-time guidance to the forecasters on the appropriate Z–R parameters for a given rainfall event. Moreover, multiple precipitation regimes often coexist within a single radar umbrella. Therefore, a physically based, automated precipitation classification process is needed. In the NMQ system, an automated precipitation classification is developed based on the 3D radar reflectivity structure and atmospheric environmental data.

The NMQ classification of precipitation regimes consists of a series of physically based heuristic rules as shown in Fig. 9. Each grid point is assigned a precipitation type based on 3D reflectivity structure and the environmental thermal and moisture fields. Currently, five precipitation types are identified: 1) stratiform rain; 2) convective rain; 3) warm rain; 4) hail; and 5) snow.

The first step in the precipitation classification is to determine if there is any precipitation at any given grid cell. If the HSR at the grid cell is above a threshold (5 dBZ if the surface temperature T_{sfc} is below 2°C and 10 dBZ otherwise), then it is considered precipitation. If T_{sfc} is below 2°C and the surface wet bulb temperature is below 0°C, then the precipitation is considered to be snow. If the precipitation is not snow, then the VILD value is checked for hail. If the VILD value exceeds 1 g m^{-3}, then the precipitation type is labeled as hail.
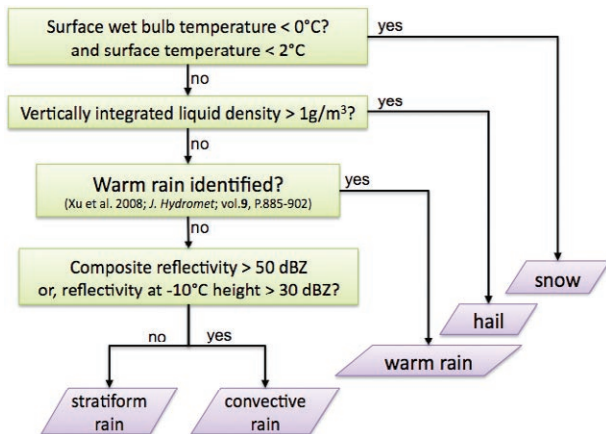
Many flash floods are caused by tropical or warm-rain processes, which are a result of high precipitation rate in relatively warm and moist atmospheric environments. Correct identification and delineation of such rain processes in radar observations are critical for the selection of a proper Z–R relationship and for accurate radar QPEs. In the NMQ system, warm rain is identified and delineated using the approach described in Xu et al. (2008). Hourly-mean volume scan VPRs from each radar are examined. If the slope of a VPR below the freezing level is negative (i.e., reflectivity increases with decreasing height), then the corresponding radar is identified as a warm-rain radar. All echoes above an adaptable threshold (default = 35 dBZ) within an influence radius of the warm-rain radar will be labeled as warm rain if they are not snow or hail and if $T_{sfc} > 10°C$. Further, any echoes above the threshold that are contiguous to the warm-rain region are defined as warm rain as well.

A convective and stratiform segregation similar to that in Zhang et al. (2008) is applied to the rest of the precipitation. A precipitation pixel is identified as convective if one of the following conditions is met: 1) reflectivity at any height in the column is greater than 50 dBZ; 2) reflectivity is greater than 30 dBZ at the −10°C height or above, or 3) one or more cloud-to-ground lightning flashes occurred in the vicinity of the pixel within the last 5 min. Temperature soundings are obtained from hourly analyses of the RUC model. The remaining echoes that are not identified as snow, hail, warm rain, or convective rain are classified as stratiform rain.

Figure 10 shows mosaicked HSR and associated precipitation type fields for two events. One event is Tropical Storm Humberto over Louisiana on 13 September 2007 (Figs. 10a,b); the other is a hailstorm that passed through Wabasha County of Minnesota in the afternoon of 13 September 2007 (Figs. 10c,d). The NMQ system identified the heavy precipitation bands around the core areas as warm-rain (Fig.10b). For the Wabasha storm event, hailstones of 3/4–1 in. were reported between 1700 and 1900 UTC and correlated well with the hail regions identified by the NMQ system (Fig. 10d).

RADAR-ONLY QPES. The precipitation classification described in the previous section provides a precipitation-type field at a high spatial (every 1 km) and temporal (every 2.5 min) resolution. This allows the radar QPE to capture small-scale variations of microphysical processes in space and in time. The NMQ radar-only precipitation

FIG. 9. Precipitation classification process in the NMQ system.

rates are obtained by applying Z–R relationships to the mosaicked HSR field pixel by pixel. Four Z–R relationships are used in association with the precipitation type field:

convective (Fulton et al. 1998): $Z = 300R^{1.4}$;　　(4)
stratiform (Marshall et al. 1955): $Z = 200R^{1.6}$;　　(5)
warm rain (Rosenfeld et al. 1993): $Z = 230R^{1.25}$; and　(6)
snow at the surface (Radar Operations Center 1999): $Z = 75R^{2.0}$.　　(7)

Here, Z represents the radar reflectivity (mm^6 m^{-3}), and R represents rain rate [Eqs. (4)–(6)] or snow water equivalent [Eq. (7); in mm h^{-1}]. The convective Z–R is capped at 55 dBZ for convective rain. It is also applied to hail pixels with a cap of 49 dBZ. A cap (default = 50 dBZ) is also applied to the warm-rain Z–R relationship.

The precipitation rate field is calculated every 2.5 min. The 1-h and 3-h accumulations are computed every 5 min by aggregating the rate fields. The hourly accumulations are aggregated into 6-, 12-, 24-, 48-, and 72-h QPE every hour at the top of the hour.

Figure 11 shows the impact of the NMQ precipitation classification and adaptive Z–R relationships on radar QPEs for a warm-rainfall event that occurred on 9 October 2009 in the Arkansas–Red Basin River Forecast Center (ABRFC) region. The operational WSR-88D 24-h rainfall (Fig. 11a) used a convective Z–R for this event, which resulted in ~35% underestimation (Fig. 11c). The Q2 radar-only QPE used a combination of warm, convective, and stratiform Z–R relationships throughout the event and produced 24-h rainfall with no bias over the ABRFC region (Fig. 11f). The Q2 radar-only rainfall verified much closer to the Oklahoma Mesonet (Brock et al. 1995) and had a much smaller root-mean-square error (RMSE; 0.75 in.) compared to the operational radar-only QPE (1.17 in.).

LOCAL GAUGE-CORRECTED RADAR QPES. The local

gauge correction (LGC) of radar QPEs in the NMQ system is based on the method developed by Ware (2005). The first step in the procedure is to calculate an additive radar rainfall error at each rain gauge location according to

$$e_i = r_i - g_i,\qquad(8)$$

where e_i is the error at the ith rain gauge, r_i is the radar-estimated rainfall, and g_i is the gauge-observed value at the ith rain gauge. Error values are then interpolated over the predefined radar domain using the following equation:

$$R_e = \left. \sum_{i=1}^{n} e_i w_i \middle/ \sum_{i=1}^{n} w_i \right. .\qquad(9)$$

Here, R_e is the estimated radar error at the pixel being interpolated, w_i is the weight assigned to the ith rain gauge, and n represents the total number of matching gauge and radar pixel pairs.

The method used to calculate the weights is a modified version of inverse distance weighting (IDW) found in Simanton and Osborn (1980). The weights are calculated with the following equation:
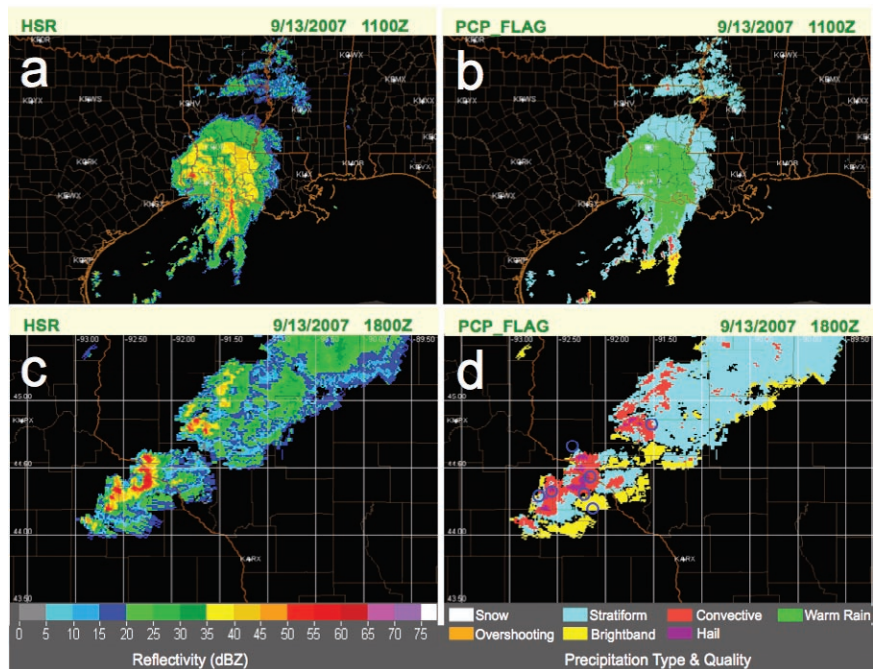

FIG. 10. (a),(c) Mosaic HSR and (b),(d) precipitation type fields for (a),(b) Tropical Storm Humberto at 1100 UTC 13 Sep 2007 and (c),(d) a hailstorm event over Wabasha, Minnesota, at 1800 UTC 13 Sep 2007. The blue circles in (d) represent surface hail reports from the NWS Storm Prediction Center valid at 1700–1900 UTC 13 Sep 2007.
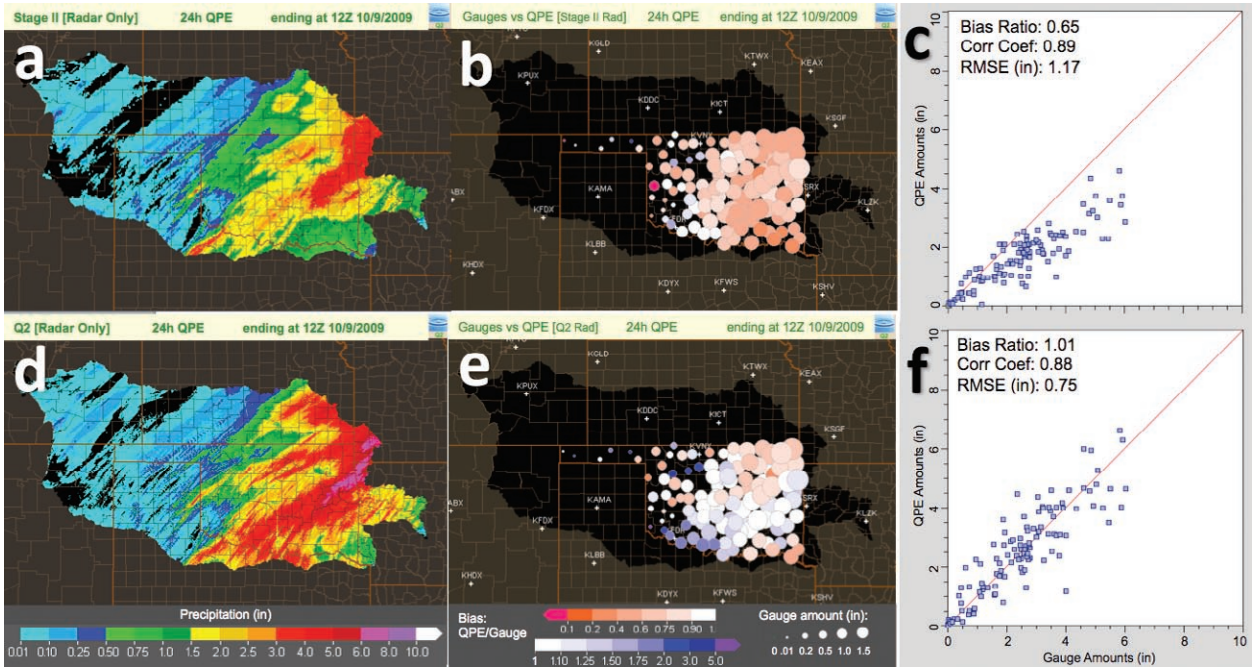
Fig. 11. Daily (a) stage II and (d) Q2 radar-only QPE maps ending at 1200 UTC 9 Oct 2009 in the ABRFC region. Bubble charts show bias ratios between (b) stage II and (e) Q2 radar-only QPEs and gauge observations, where the size of the circles represents the gauge-observed rainfall amount and the color shows the bias. Scatterplots show distributions of the 24-h (c) stage II and (f) Q2 radar-only QPEs vs the gauge observations.

$$w_i = \begin{cases} 1\!\!\big/\!d_i^b & d_i \leq D \\ 0; & d_i > D \end{cases}, \qquad (10)$$

where d_i is the distance between the radar pixel and the ith rain gauge, b is an exponent, and n is the number of rain gauges within a specified radius D of the radar pixel. In a dense rain gauge network, rain gauges that are located far from the radar pixel will have large distances and small weights and will have little effect on the error estimate. However, in regions with sparse gauges, sometimes only one gauge can be used in the interpolation, resulting in a constant error within the entire radius of influence. This problem can be alleviated by applying a normal distribution to the error estimates in which the gauge impact is reduced as the distance away from that gauge increases. For each radar pixel, the following value is calculated:

$$\alpha = \sum_{i=1}^{n} \exp\!\left(\frac{-d_i^2}{(D/2)^2} \right). \qquad (11)$$

Here, D is the radius of influence and n is the number of rain gauges within the specified radius D of the radar pixel. If the value is greater than 1, then there are a sufficient number of gauges being used to

interpolate that point. If the value is less than 1, then the radar estimate is given the remaining weight to equal 1 and the following equation is used for the weighting function:

$$w_i = \begin{cases} \alpha \times \dfrac{1}{d_i^b}; & d_i \leq D \\ 0; & d_i > D \end{cases}, \qquad (12)$$

where all variables are the same as defined above. This procedure results in more weight being given to the radar estimates in areas of poor rain gauge coverage and at domain boundaries.

Values of the exponent b and the influence radius D in Eqs. (10) and (12) are obtained by minimizing the mean squared (radar–gauge) error (MSE) using a cross-validation scheme. Initial values of b and D are selected, and the cross validation is performed by removing a rain gauge and interpolating to its location using radar–gauge errors at all the remaining rain gauges. The difference between the interpolated radar–gauge error and the observed value is then calculated. After cross validating all rain gauge points, a total cross-validated MSE is calculated. The two parameters are then adjusted to a new set of trial values and the cross-validation process is repeated. The trial values for D can range from ~10 to 500 km with an adjustment interval of 10 km, and b can range

from 0.5 to 3.0 with an adjustment interval of 0.5. Thus, there are 50 × 6 = 300 possible combinations of the parameters. The combination that produces minimum cross-validated MSE is considered the best. Cross validation is performed for each analysis time (i.e., every hour), resulting in different optimum parameters each time.

Anomalously high or low rain gauge values tend to influence adjacent points in the error field because of the nature of interpolation. To remedy this problem, a quality-control step is applied to the gauge data. This step removes rain gauges that strongly disagree with the surrounding observations so that a spatially consistent precipitation map can be obtained after the local bias correction. For each rain gauge location, all error estimates at radar pixels within a radius of ~10 km are compared with the error value at the gauge. If less than 25% of those error estimates are within a difference threshold ΔR (default = 5 mm) of the error at the gauge, then the rain gauge is considered problematic. The problematic rain gauges are removed and cross validation is rerun, which often results in a new set of IDW parameter values. The same procedure is repeated using a smaller difference threshold (e.g., 4 mm) and two more iterations follow, with cross-validation running between iterations. To ensure that a large number of rain gauges are not eliminated, the pro-cedure is terminated if more than 10% of the total number of gauges are omitted.

Figure 12 shows example Q2 24-h radar QPEs with and without the LGC, where the HADS hourly gauges were used in the correction. The Q2 radar-only and LGC radar QPEs are compared with the Oklahoma Mesonet gauges that were not used in the LGC. The Q2/gauge bias-ratio maps (Figs. 12b,e) showed that the LGC increased the rainfall estimates in the northeastern and southeastern corners of Oklahoma and reduced those near the southwestern Oklahoma border. The LGC increased the correlation coefficient from 0.88 (Fig. 12c) to 0.95 (Fig. 12f) and reduced the root-mean-square error from 0.75 (Fig. 12c) to 0.49 (Fig. 12f).

Q2 MOUNTAIN MAPPER. In complex terrains, the accuracy of radar QPE is limited by several factors, such as beam blockage and overshooting (Maddox et al. 2002), vertical reflectivity profile variation (Joss and Waldvogel 1990; Germann and Joss 2002), and orographic enhancement (Kitchen et al. 1994). The problem is more pronounced for the cool-season stratiform precipitation than for deep convective precipitation because the former has relatively low cloud tops. To address this issue, a special technique named Mountain Mapper (MM; Schaake et al. 2004) is used by several River Forecast Centers (RFC) in the western United States. The MM technique is based on real-
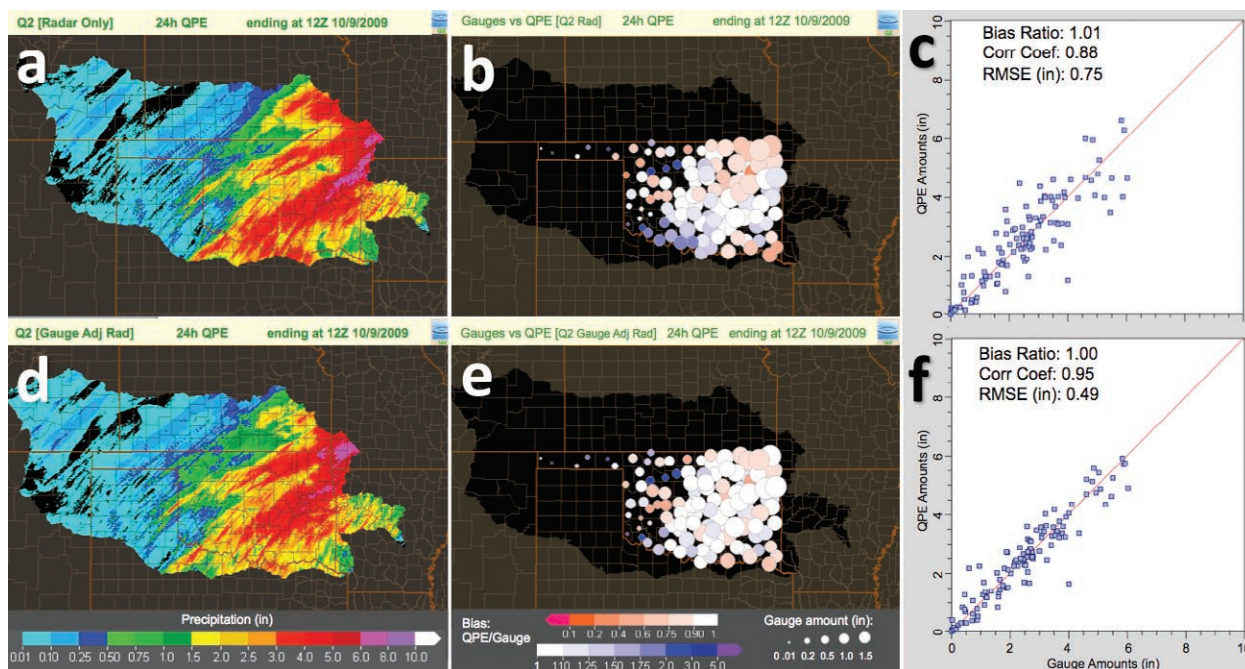

FIG. 12. Daily Q2 radar QPE maps ending at 1200 UTC 9 Oct 2009 in the ABRFC region (a) before and (d) after the local gauge bias correction. (b),(e) Bubble charts show bias ratios between the Q2 radar QPEs and independent gauge observations, where the size of the circles represents the gauge-observed rainfall amount and the color shows the bias. (c),(f) Scatterplots show distributions of the 24-h Q2 QPEs vs the gauge observations.

time gauge observations and a background rainfall distribution map derived from Parameter-Elevation Regressions on Independent Slopes Model (PRISM; Daly et al. 1994; www.prism.oregonstate.edu/). PRISM is a unique analytical tool that uses point measurements of precipitation, temperature, a digital elevation model (i.e., terrain height), and expert knowledge of complex climatic features (e.g., rain shadows and coastal effects) to produce continuous, digital grid estimates of monthly, yearly, and event-based climatic parameters. Below is a brief description of the Q2 MM procedure:

1) Scale down a specific PRISM monthly precipitation climatology into an hourly rainfall field by dividing the monthly precipitation by the number of hours in the month.
2) Compute the ratio (G/P) of hourly gauge rainfall G and the normalized PRISM hourly rainfall P at each gauge site.
3) Interpolate the ratio field onto the Q2 analysis grid using an inverse distance-squared weighting function.
4) Multiply the gridded ratio field by the scaled PRISM hourly rainfall field, and the result is the MM hourly analysis.

In the Q2 system, HADS (www.weather.gov/oh/hads/) hourly gauge data are used for generating Q2 MM rainfall products. Figure 13 shows 24-h
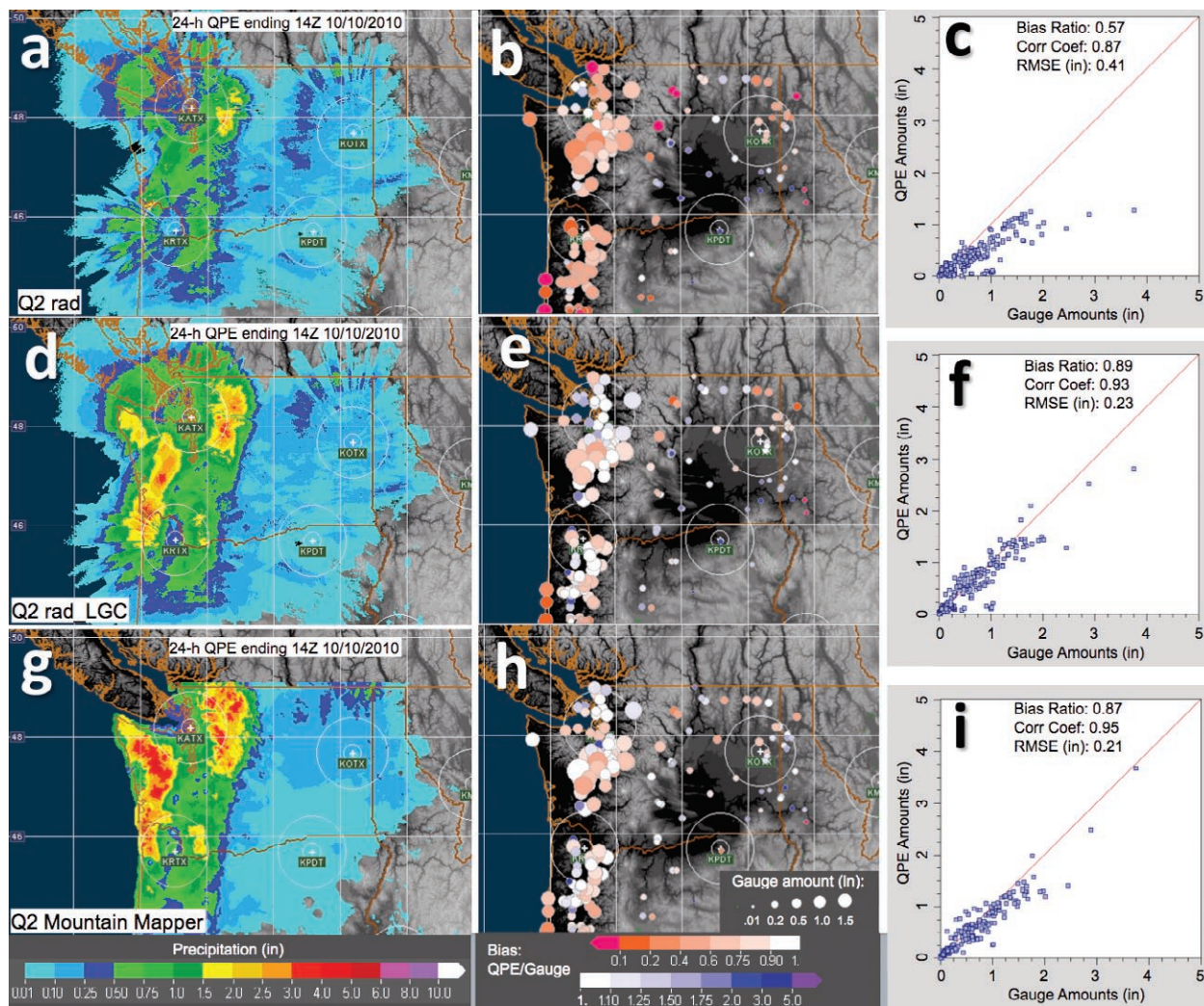

FIG. 13. 24-h accumulations of (a) Q2 radar, (d) Q2 LGC radar, and (g) Q2 MM QPEs ending at 1400 UTC 10 Oct 2010 in the Pacific Northwest region. Q2MM QPE uses only HADS gauges as input. (b),(e),(h) Bubble charts show the bias ratios between the three different Q2 products and CoCoRaHS gauge observations, where the circle size represents gauge-observed amount and color represents the Q2/gauge bias. (c),(f),(i) Scatterplots show the correlation between the Q2-estimated and gauge-observed amounts.

Q2 products ending at 1400 UTC 10 October 2010 over the Pacific Northwest region. The Q2 radar-only QPE (Figs. 13a–c) underestimated the domain-average rainfall by more than 40% and had a domain-average RMSE of 0.41 in. The radar rainfall map (Fig. 13a) exhibited nonphysical discontinuities and artifacts because of terrain blockages. After the local gauge bias correction, there was much less underestimation (11%) and smaller RMSE (0.23 in). However, the blockage artifacts remained (Fig. 13d). The Q2 MM gauge-based rainfall map (Fig. 13g) was free of the radar sampling artifacts, and it had a similar bias ratio, a slightly higher correlation coefficient (0.95 vs 0.93), and a lower RMSE (0.21 in. vs 0.23 in) than the Q2 local gauge bias-corrected radar QPE. This example indicates the great potential of the MM technique in areas of complex terrain for cool-season stratiform precipitation. However, the MM does not perform as well for small-scale convective precipitation, given its dependency on gauges. Figure 14 shows a convective precipitation event that occurred in Arizona during the monsoon season. Both Q2 radar QPE (Figs. 14a–c) and Q2 LGC radar QPE (Figs. 14d–f) performed better than the Q2 MM QPE (Figs. 14g–i).

The MM directly uses real-time rain gauge observations and the PRISM climatology maps to derive precipitation estimates; thus, it implicitly accounts for flow regimes and terrain-blocking effects. However, the accuracy of the MM QPE depends on the real-time gauge densities with respect to the precipitation scale and differences between the PRISM climatology and the real-time precipitation regime. For small-scale precipitation events and a sparse gauge network, certain precipitation features may not be observed (e.g., the event shown in Fig. 14). When the real-time precipitation distribution is largely different than the PRISM climatology, the MM QPE could have a large error. Atmospheric environmental data may be better suited to define the real-time precipitation regimes than the PRISM climatology, and further studies are needed to quantify the relationship between
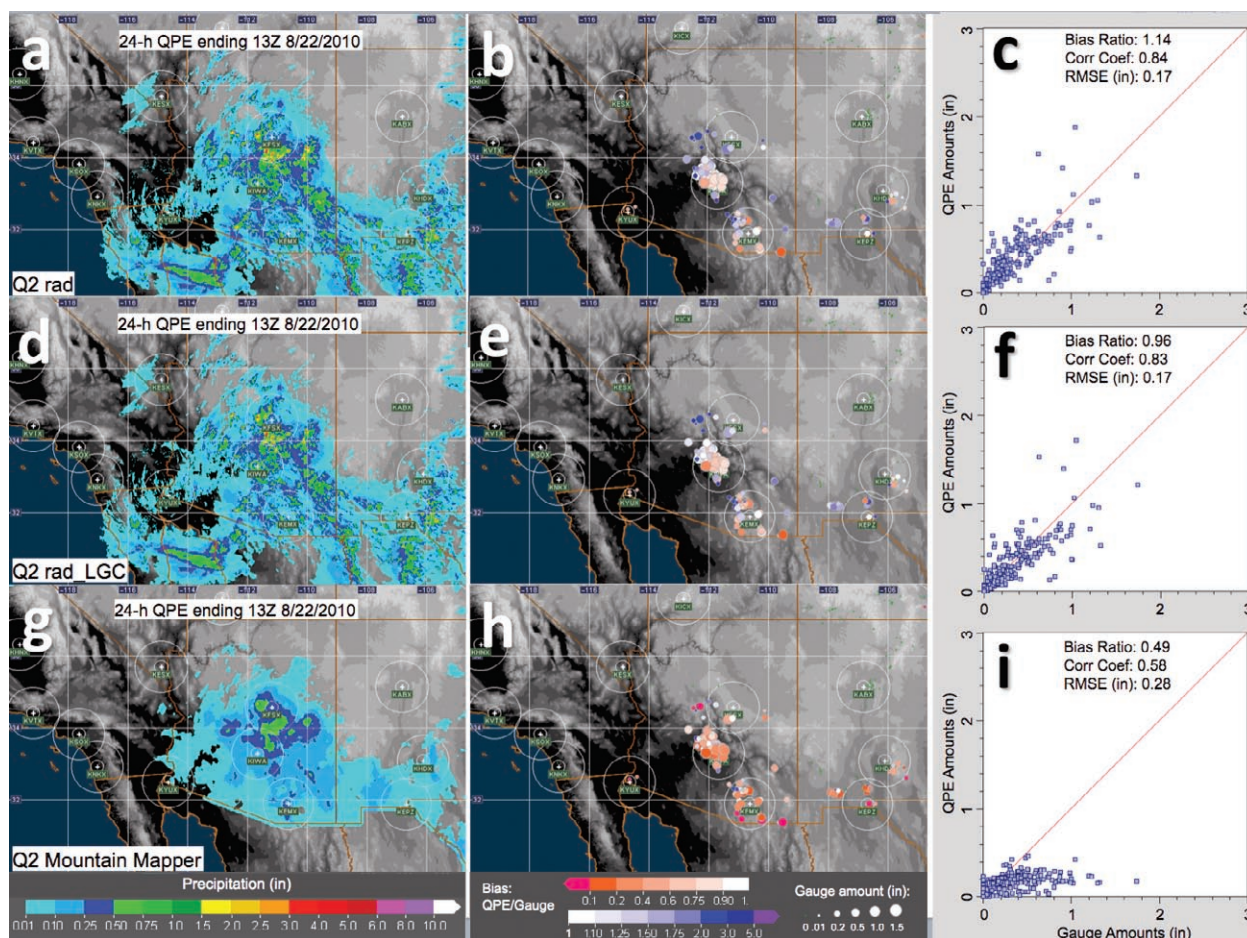

FIG. 14. As in Fig. 13, but for 24-h rainfall accumulations ending at 1300 UTC 22 Aug 2010 in the southwestern United States.

atmospheric environmental variables and the precipitation amount on the ground.

Evaluations and applications. The NMQ system contains a display and verification system called the NMQ Verification System (QVS; see sidebar), where all the products can be viewed in real time from the public Web site (http://nmq.ou.edu) as images with various geographic information overlays (e.g., political boundaries, radar sites and range rings, topography, and RFC and county warning area boundaries). All product images presented in this paper were obtained from the QVS Web site. The NMQ precipitation products can be compared with rain gauge observations from HADS, the Community Collaborative Rain, Hail and Snow Network (CoCoRaHS; www.cocorahs. org), and several local Mesonet rain gauge networks. Various statistics, such as bias, correlation coefficient, and root-mean-square error, are computed between QPE products and independent rain gauge observations (e.g., Figs. 11–14). Operational precipitation products from various sensors, including stage II, stage IV (Lin and Mitchell 2005), and the Hydro-Estimator (Scofield and Kuligowski 2003), are also incorporated in the QVS for real-time intercomparisons. Through these intercomparisons and evaluations of multisensor QPEs, a better understanding of the uncertainties associated with each QPE can be obtained, providing scientific insights toward an optimally merged multisensor QPE.

A running 3-yr archive of key NMQ products (Table 1) is kept online in the QVS. Users from government agencies, universities, and private sectors have employed the experimental NMQ products in various applications. The 3D reflectivity mosaic component has been implemented at the National Centers for Environmental Prediction (NCEP) for operational data assimilation in the RUC model. It was shown

TABLE 1. List of NMQ products.			
ID	**Unit**	**Update cycle**	**Description**
UNQC_CREF	dBZ	5 min	Non-quality-controlled composite reflectivity
MREF3D	dBZ	2.5 min	3D mosaicked reflectivity field
CREF	dBZ	2.5 min	Composite reflectivity
CREFH	km MSL	2.5 min	Height of composite reflectivity
HSR	dBZ	2.5 min	Hybrid scan reflectivity
HSRH	km above ground	2.5 min	Height of hybrid scan reflectivity
ETPI8	km MSL	2.5 min	Echo top of 18 dBZ
SHI	none	2.5 min	Severe hail index
POSH	%	2.5 min	Possibility of severe hail
MEHS	mm	2.5 min	Max expected hail size
VIL	kg m^{-2}	2.5 min	Vertically integrated liquid
VILD	g m^{-3}	2.5 min	VIL density
PCP_FLAG	none	2.5 min	Precipitation type
PCP_RATE	mm h^{-1}	2.5 min	Precipitation rate
Q2RAD_HSR_1(3)H	mm	2.5 min	1-h (3 h) radar-derived precipitation accumulations
Q2RAD_HSR_6(12,24, 48, 72)H	mm	1 h, at the top of the hour	6-h (12, 24, 48, 72 h) radar-derived precipitation accumulations
Q2GC_HSR_1(3,6,12, 24, 48, 72)H	mm	1 h, at the top of the hour	1-h (3, 6, 12, 24, 48, 72 h) local gauge-corrected radar precipitation accumulations
Q2GAUGE_1(3,6,12, 24, 48, 72)H	mm	1 h, at the top of the hour	1-h (3, 6, 12, 24, 48, 72 h) gauge precipitation accumulations
Q2MM_1(3,6,12, 24,48, 72)H	mm	1 h, at the top of the hour	1-h (3, 6, 12, 24, 48, 72 h) gauge-, terrain-, and climatology-based precipitation accumulations

that assimilating 3D reflectivity data significantly improved the 0–6-h quantitative precipitation forecasts (Weygandt et al. 2007). The 3D reflectivity mosaic is also used in aviation icing severity analysis (Serke et al. 2008). The 2D composite reflectivity (CREF) product has been used by Fabry and Seed (2007) for a storm predictability study.

The precipitation products are compared to satellite QPEs from the Tropical Rainfall Measurement Mission (Amitai 2009). In 2006, working with the NWS Office of Climate, Weather, and Water Services, NSSL began prototype testing of the high-resolution gridded Q2 precipitation products as input into the Flash Flood Monitoring and Prediction program. Dissemination of NMQ QPE products to selected RFCs began in 2007 with all RFCs currently having access through a new Advanced Weather Interactive Processing System (AWIPS) build for MPE. Several RFCs, including the West Gulf, Southeast, Ohio, and North Central are now using the NMQ radar rainfall products in their operations. Hydrometeorological analysis and support forecasters manually edit radar and gauge data on an hourly basis and have found several benefits of NMQ data to their operations. For example, the NMQ automated QC saves valuable time editing nonprecipitating echoes from hourly QPEs. Other benefits to the RFCs are increased range coverage from 230 to 460 km, mitigation of boundary artifacts combining the products from individual radars, and the dynamic Z–R.

Collaborations are ongoing to assess the utility of NMQ precipitation products in operational hydrological models (Wu and Kitzmiller 2009). In coordination with RFCs, several weather forecast offices (WFO) are beginning to experiment with NMQ data in their Site Specific Headwater Predictor model.

CHALLENGES AND FUTURE PLANS.
Although the NMQ products provide improvements over existing operational radar QPE products, there are still challenges and unresolved issues. Summarized below are the remaining challenges that face the NMQ and future work that will potentially address the challenges.

Reflectivity quality-control challenges. One challenge that faces the current NMQ radar data QC is the difficulty of identifying deep blooms, especially when the temperature is relatively cold (e.g., in early spring or late fall). The heuristic bloom QC scheme is turned off when the temperature at the radar site is below 5°C. Snow could occur under this condition, and its spatial characteristics are similar to the blooms. Another challenge is the removal of AP echoes at far

THE QVS

An integral part of the NMQ effort is the Web page (http://nmq.ou.edu) referred to as the NMQ Verification System (QVS). The QVS provides equal ease of access to imagery minutes old to 3 yr old and so acts as both a real-time monitoring system and a case study platform. Behind the QVS lies a multiterabyte archive of roughly 3 yr of high-resolution national 3D radar mosaic, severe storm, and QPE data. A variety of methods, tools, and screening procedures are available on the QVS for viewing and analyzing both the products and incoming datasets (e.g., model and satellite). One focus of the QVS is the QPE products verification, including 2D maps of color-coded QPE bias and gauge amount circles, scatter plots, and multivariable time series plots for any point in the entire grid.

The QVS goes beyond a Web page of static image links but rather functions as a Web portal for powerful real-time image generation software. Image generation "on the fly" allows for a vast parameter space of user-selectable settings, including various geospatial information overlays. For instance, a vertical cross section through the 3D radar reflectivity mosaic can be generated between two arbitrary latitude/longitude end points anywhere in the conterminous United States for any time in the last 3 yr. Such a capability appears at this time to be unique among publically accessible online hydrometeorological resources.

ranges, where small convective cells could be present and have similar local structure. To avoid the erroneous removal of snow or small storms at far ranges, the NMQ algorithm tends to leave these bloom or AP echoes in the data, resulting in false precipitation.

These issues will hopefully be addressed with dual-polarization radar capabilities (e.g., Ryzhkov et al. 2005; Park et al. 2009), where additional radar variables can be used to better identify different scatterers. In sync with the polarimetric upgrade of the WSR-88D network, future NMQ work will include the integration of polarimetric radar data QC techniques.

Data gaps in the WSR-88D radar network. The challenge with the NMQ 3D radar reflectivity mosaic ties to the scanning strategy of the WSR-88Ds. There are data voids below the lowest tilt and above the highest tilt (i.e., the "cone of silence"). Further, the vertical resolution becomes very coarse (beam size expanding) at far ranges. As a result, discontinuities may appear in the 3D reflectivity mosaic fields at the heights where strong vertical reflectivity gradients exist (e.g., BB layer boundaries and cloud top). In collaboration with the NOAA/HMT, gap-filling radars will be

integrated into the NMQ system to fill in some of the WSR-88D data gaps. Future space borne radars, such as those from the Global Precipitation Measurement (GPM; http://gpm.gsfc.nasa.gov) satellites, can provide additional coverage, and integrations of such data into the NMQ will be explored.

Radar QPE errors associated with nonuniform VPRS. The data voids below the lowest radar tilt and the beam expanding are also a cause of radar QPE errors because of nonuniform VPRs. The current VPR correction in NMQ can only address such errors associated with relatively large-scale and horizontally uniform stratiform precipitation. Accurate VPR correction for radar QPEs in complex terrain, especially in the cool season, remains an unresolved issue. Several ongoing efforts in the NMQ R&D are focused on this issue, which include the study of high-resolution precipitation profiler data to improve understanding of vertical precipitation structure in complex terrain and the exploration of using space borne radar VPRs to correct the ground radar QPE. A merged product using the Q2 radar, Q2 MM, and atmospheric environmental fields is also underway.

Radar QPE uncertainties associated with precipitation classifications and Z–R relationships. Currently, four Z–R relationships are used in NMQ to derive the precipitation rate from radar data across the CONUS for all seasons. However, variations of the Z–R relationship over such large space and time scales can exceed the realm of what these four Z–R relationships could represent. Further, the current precipitation classification is relatively simplistic, and some error sources (e.g., wind shear–induced drifting, relative locations of cloud-to-ground lightning, and convective precipitation) are yet to be accurately accounted for. Evaluations of the NMQ precipitation products indicated that the current tropical Z–R relationship could still underestimate rainfall intensities in very deep, warm, and moist environments. An effort has started to integrate polarimetric radar QPE techniques into the NMQ system, and the error associated with Z–R uncertainties is expected to decrease because additional polarimetric radar variables can be used for hydrometeor classifications (e.g., Ryzhkov et al. 2005; Giangrande and Ryzhkov 2008). Meanwhile, the NMQ system can serve as a platform for real-time evaluations of the NWS operational dual-polarization QPE products over CONUS and can facilitate the advancement of dual-polarization radar QPE techniques.

Evaluations and advancements of NMQ. Along with integrations of new technologies and new data, systematic evaluations of the NMQ products will continue. The quality assurance of ground truth data, especially for winter precipitation, remains a huge challenge for quantitative evaluations of remote sensing QPEs. This further asserts the value of RFC forecasters' work in gauge quality assurance. One effort is underway to compare NMQ products with the stage IV product because of the vigorous quality control that went into the latter product. Further, event-based evaluations by NWS forecasters and by the general public continue to provide valuable guidance to the NMQ R&D efforts and facilitate advances of the QPE science and technologies that are beneficial to the NWS operations.

REFERENCES

Amburn, S. A., and P. L. Wolf, 1997: VIL density as a hail indicator. *Wea. Forecasting,* **12,** 473–478.

Amitai, E., 2009: Comparison of TRMM radar rainfall estimates with NOAA next-generation QPE. *J. Meteor. Soc. Japan,* **87A,** 109–118.

Bellon, A., G.-W. Lee, and I. Zawadzki, 2005: Error statistics of VPR corrections in stratiform precipitation. *J. Appl. Meteor.,* **44,** 998–1015.

Benjamin, S. G., and Coauthors, 2004: An hourly assimilation–forecast cycle: The RUC. *Mon. Wea. Rev.,* **132,** 495–518.

Brock, F. V., K. C. Crawford, R. L. Elliott, G. W. Cuperus, S. J. Stadler, H. L. Johnson, and M. D. Eilts, 1995: The Oklahoma Mesonet: A technical overview. *J. Atmos. Oceanic Technol.,* **12,** 5–19.

Crum, T. D., and R. L. Alberty, 1993: The WSR-88D and the WSR-88D operational support facility. *Bull. Amer. Meteor. Soc.,* **74,** 1669–1687.

——, D. Evancho, C. Horvat, M. Istok, and W. Blanchard, 2003a: An update on NEXRAD program plans for collecting and distributing WSR-88D base data in near real time. Preprints, *19th Conf. on Interactive*

Information Processing Systems (IIPS) for Meteorology, Oceanography, and Hydrology, Long Beach, CA, Amer. Meteor. Soc., 14.2. [Available online at http://ams.confex.com/ams/pdfpapers/56479.pdf.]

——, and Coauthors, 2003b: Progress in implementing near-real time collection, distribution, and archive of WSR-88D level II data. Preprints, *31st Conf. on Radar Meteorology,* Seattle, WA, Amer. Meteor. Soc., 12B.3. [Available online at http://ams.confex.com/ams/pdfpapers/63127.pdf.]

Daly, C., R. P. Neilson, and D. L. Phillips, 1994: A statistical–topographic model for mapping climatological precipitation over mountainous terrain. *J. Appl. Meteor.,* **33,** 140–158.

Droegemeier, K. K., and Coauthors, 2002: Project CRAFT: A test bed for demonstrating the real time acquisition and archival of WSR-88D level II data, Preprints, *18th Int. Conf. on Interactive Information Processing Systems (IIPS) for Meteorology, Oceanography, and Hydrology,* Orlando, FL, Amer. Meteor. Soc., 5.20. [Available online at http://ams.confex.com/ams/pdfpapers/30900.pdf.]

Fabry, F., and A. Seed, 2007: Quantifying and predicting the accuracy of radar based quantitative precipitation forecasts. Preprints, *33rd Int. Conf. on Radar Meteorology,* Cairns QLD, Australia, Amer. Meteor. Soc., P6B.5. [Available online at http://ams.confex.com/ams/pdfpapers/122924.pdf.]

Fulton, R., J. Breidenbach, D.-J. Seo, D. Miller, and T. O'Bannon, 1998: The WSR-88D rainfall algorithm. *Wea. Forecasting,* **13,** 377–395.

Germann, U., and J. Joss, 2002: Mesobeta profiles to extrapolate radar precipitation measurements above the Alps to the ground level. *J. Appl. Meteor.,* **41,** 542–557.

Giangrande, S. E., and A. V. Ryzhkov, 2008: Estimation of rainfall based on the results of polarimetric echo classification. *J. Appl. Meteor. Climatol.,* **47,** 2445–2462.

Glaudemans, M., P. Tilles, and B. Lawrence, 2008: Interactive quality control and operational product generation of hourly multi-sensor precipitation estimates in the NWS. Preprints, *25th Conf. on Int. Interactive Information and Processing Systems (IIPS) for Meteorology, Oceanography, and Hydrology,* Phoenix, AZ, Amer. Meteor. Soc., 5B.3. [Available online at http://ams.confex.com/ams/pdfpapers/143861.pdf.]

Gourley, J. J., J. Zhang, R. A. Maddox, C. M. Calvert, and K. W. Howard, 2001: A real-time precipitation monitoring algorithm—Quantitative precipitation estimation and segregation using multiple sensors (QPE SUMS). Preprints, *Symp. on Precipitation Extremes: Prediction, Impacts, and Responses,* Albuquerque, NM, Amer. Meteor. Soc., 57–60.

——, R. A. Maddox, K. W. Howard, and D. W. Burgess, 2002: An exploratory multisensor technique for quantitative estimation of stratiform rainfall. *J. Hydrometeor.,* **3,** 166–180.

Greene, D. R., and R. A. Clark, 1972: Vertically integrated liquid water—A new analysis tool. *Mon. Wea. Rev.,* **100,** 548–552.

Joss, J., and A. Waldvogel, 1990: Precipitation measurements and hydrology. *Radar in Meteorology,* D. Atlas, Ed., Amer. Meteor. Soc., 577–606.

Kelleher, K. E., and Coauthors, 2007: Project CRAFT: A real-time delivery system for NEXRAD level II data via the Internet. *Bull. Amer. Meteor. Soc.,* **88,** 1045–1057.

Kitchen, M., R. Brown, and A. G. Davies, 1994: Real-time correction of weather radar data for the effects of bright band, range and orographic growth in widespread precipitation. *Quart. J. Roy. Meteor. Soc.,* **120,** 1231–1254.

Koistinen, J., 1991: Operational correction of radar rainfall errors due to the vertical reflectivity profile. Preprints, *25th Int. Conf. on Radar Meteorology,* Paris, France, Amer. Meteor. Soc., 91–94.

Lakshmanan, V., T. Smith, K. Hondl, G. J. Stumpf, and A. Witt, 2006: A real-time, three-dimensional, rapid updating, heterogeneous technique radar merger technique for reflectivity, velocity, and derived products. *Wea. Forecasting,* **21,** 802–823.

——, A. Fritz, T. Smith, K. Hondl, and G. J. Stumpf, 2007: An automated technique to quality control radar reflectivity data. *J. Appl. Meteor. Climatol.,* **46,** 288–305.

——, J. Zhang, and K. Howard, 2010: A technique to censor biological echoes in weather radar images. *J. Appl. Meteor. Climatol.,* **49,** 453–462.

Langston, C., J. Zhang, and K. Howard, 2007: Four-dimensional dynamic radar mosaic. *J. Atmos. Oceanic Technol.,* **24,** 776–790.

Lin, Y., and K. E. Mitchell, 2005: The NCEP stage II/IV hourly precipitation analyses: Development and applications. Preprints, *19th Conf. on Hydrology,* San Diego, CA, Amer. Meteor. Soc., 1.2. [Available online at http://ams.confex.com/ams/pdfpapers/83847.pdf.]

Maddox, R., J. Zhang, J. Gourley, and K. Howard, 2002: Weather radar coverage over the contiguous United States. *Wea. Forecasting,* **17,** 927–934.

Marshall, J. S., W. Hitschfeld, and K. L. S. Gunn, 1955: Advances in radar weather. *Advances in Geophysics,* Vol. 2, Academic Press, 1–56.

McLaughlin, D. J., and Coauthors, 2005: Distributed Collaborative Adaptive Sensing (DCAS) for improved detection, understanding and prediction

of atmospheric hazards. *Proc. Ninth Symp. on Integrated Observing and Assimilation Systems for the Atmosphere, Oceans, and Land Surface (IOAS-AOLS),* San Diego, CA, Amer. Meteor. Soc., 11.3. [Available online at http://ams.confex.com/ams/pdfpapers/87890.pdf.]

O'Bannon, T., 1997: Using a "terrain-based" hybrid scan to improve WSR-88D precipitation estimates. Preprints, *28th Int. Conf. on Radar Meteorology,* Austin, TX, Amer. Meteor. Soc., 506–507.

Park, H. S., A. V. Ryzhkov, D. S. Zrnić, and K.-E. Kim, 2009: The hydrometeor classification algorithm for the polarimetric WSR-88D: Description and application to an MCS. *Wea. Forecasting,* **24,** 730–748.

Radar Operations Center, 1999: Guidance on selecting Z–R relationships. [Available online at www.roc.noaa.gov/ops/z2r_osf5.asp.]

Rosenfeld, D., D. B. Wolff, and D. Atlas, 1993: General probability-matched relations between radar reflectivity and rain rate. *J. Appl. Meteor.,* **32,** 50–72.

Ryzhkov, A. V., T. J. Schuur, D. W. Burgess, P. L. Heinselman, S. E. Giangrande, and D. S. Zrnić, 2005: The Joint Polarization Experiment: Polarimetric rainfall measurements and hydrometeor classification. *Bull. Amer. Meteor. Soc.,* **86,** 809–824.

Schaake, J., A. Henkel, and S. Cong, 2004: Application of PRISM climatologies for hydrologic modeling and forecasting in the western U.S. Preprints, *18th Conf. on Hydrology,* Seattle, WA, Amer. Meteor. Soc., 5.3. [Available online at http://ams.confex.com/ams/pdfpapers/72159.pdf.]

Scofield, R. A., and R. J. Kuligowski, 2003: Status and outlook of operational satellite precipitation algorithms for extreme-precipitation events. *Wea. Forecasting,* **18,** 1037–1051.

Seo, D.-J., J. Breidenbach, R. Fulton, D. Miller, and T. O'Bannon, 2000: Real-time adjustment of range-dependent biases in WSR-88D rainfall estimates due to nonuniform vertical profile of reflectivity. *J. Hydrometeor.,* **1,** 222–240.

Serke, D., F. McDonough, and M. K. Politovich, 2008: Analysis of 3-D NEXRAD mosaic reflectivity data colocated with research aircraft and satellite data: Implications on in-flight icing. Preprints, *13th Conf. on Aviation, Range and Aerospace Meteorology,* New Orleans, LA, Amer. Meteor. Soc., P4.8. [Available online at http://ams.confex.com/ams/pdfpapers/128224.pdf.]

Simanton, J. R., and H. B. Osborn, 1980: Reciprocal distance estimate of point rainfall. *J. Hydraul. Div. Amer. Soc. Civ. Eng.,* **106,** 1242–1246.

Vasiloff, S. V., and Coauthors, 2007: Improving QPE and very short term QPF: An initiative for a community-wide integrated approach. *Bull. Amer. Meteor. Soc.,* **88,** 1899–1911.

Vignal, B., H. Andrieu, and J. D. Creutin, 1999: Identification of vertical profiles of reflectivity from volume-scan radar data. *J. Appl. Meteor.,* **38,** 1214–1228.

——, G. Galli, J. Joss, and U. Germann, 2000: Three methods to determine profiles of reflectivity from volumetric radar data to correct precipitation estimates. *J. Appl. Meteor.,* **39,** 1715–1726.

Ware, E. C., 2005: Corrections to radar-estimated precipitation using observed rain gauge data. M.S. thesis, Cornell University, 87 pp. [Available from Cornell University Library, 201 Olin Library, Cornell University, Ithaca, NY 14853-5301.].

Weygandt, S. S., S. G. Benjamin, and J. M. Brown, 2007: Radar reflectivity-based initialization of precipitation systems using a diabatic digital filter. Preprints, *33rd Int. Radar Conf.,* Cairns QLD, Australia, Amer. Meteor. Soc., 4A.6. [Available online at http://ams.confex.com/ams/pdfpapers/123697.pdf.]

Witt, A., M. D. Eilts, G. J. Stumpf, J. T. Johnson, E. D. Mitchell, and K. W. Thomas, 1998: An enhanced hail detection algorithm for the WSR-88D. *Wea. Forecasting,* **13,** 286–303.

Wu, W., and D. Kitzmiller, 2009: Evaluation of radar precipitation estimates from NMQ and WSR-88D digital precipitation array products: Preliminary results. Preprints, *34th Conf. on Radar Meteorology,* Williamsburg, VA, Amer. Meteor. Soc., P14.4. [Available online at http://ams.confex.com/ams/pdfpapers/155669.pdf.]

Xu, X., K. Howard, and J. Zhang, 2008: An automated radar technique for the identification of tropical precipitation. *J. Hydrometeor.,* **9,** 885–902.

Zhang, J., and Y. Qi, 2010: A real-time algorithm for the correction of brightband effects in radar-derived precipitation estimation. *J. Hydrometeor.,* **11,** 1157–1171.

——, S. Wang, and B. Clarke, 2004: WSR-88D reflectivity quality control using horizontal and vertical reflectivity structure. Preprints, *11th Conf. on Aviation, Range, and Aerospace Meteorology,* Hyannis, MA, Amer. Meteor. Soc., 5.4. [Available online at http://ams.confex.com/ams/pdfpapers/81858.pdf.]

——, K. Howard, and J. J. Gourley, 2005: Constructing three-dimensional multiple radar reflectivity mosaics: Examples of convective storms and stratiform rain echoes. *J. Atmos. Oceanic Technol.,* **22,** 30–42.

——, C. Langston, and K. Howard, 2008: Brightband identification based on vertical profiles of reflectivity from the WSR-88D. *J. Atmos. Oceanic Technol.,* **25,** 1859–1872.